

Toward Low Temperature Solid-Source Synthesis of Monolayer MoS₂

Alvin Tang^{1,†}, Aravindh Kumar^{1,†}, Marc Jaikissoon¹, Krishna Saraswat^{1,2,3}, H.-S. Philip Wong^{1,3}, and Eric Pop^{1,2,3*}

¹Department of Electrical Engineering, Stanford University, Stanford, CA, 94305, USA

²Department of Materials Science and Engineering, Stanford University, Stanford, CA, 94305, USA

³Precourt Institute for Energy, Stanford University, Stanford, CA, 94305, USA

[†]Authors contributed equally.

*To whom correspondence should be addressed: epop@stanford.edu

ABSTRACT

Two-dimensional (2D) semiconductors have been proposed for heterogeneous integration with existing silicon technology, however their chemical vapor deposition (CVD) growth temperatures are often too high. Here, we demonstrate direct CVD solid source precursor synthesis of continuous monolayer (1L) MoS₂ films at 560°C in 50-minutes, within the 450-to-600°C, 2-hour thermal budget window required for back-end-of-the-line (BEOL) compatibility with modern silicon technology. Transistor measurements reveal on-state current up to ~140 $\mu\text{A}/\mu\text{m}$ at 1 V drain-to-source voltage for 100 nm channel lengths, the highest reported to date for 1L MoS₂ grown below 600°C using solid source precursors. The effective mobility from transfer length method (TLM) test structures is $29 \pm 5 \text{ cm}^2\text{V}^{-1}\text{s}^{-1}$ at $6.1 \times 10^{12} \text{ cm}^{-2}$ electron density, which is comparable to mobilities reported from films grown at higher temperatures. The results of this work provide a path towards the realization of high quality, thermal-budget-compatible 2D semiconductors for heterogeneous integration with silicon manufacturing.

KEYWORDS: 2D materials, transition metal dichalcogenides, MoS₂, molybdenum disulfide, BEOL, back-end-of-the-line, chemical vapor deposition, CVD growth, carrier mobility

Since the era of the first integrated circuits, improving semiconductor device density has continuously translated into benefits for more advanced computing systems.¹ The horizontally stacked gate-all-around (GAA) nanosheet transistor with 3 nm thick Si nanosheets is expected to replace the FinFET structure to continue transistor scaling beyond the 5 nm technology node.² However, further gate length scaling or better control over off-state leakage requires thinner body channel materials,³ making atomically thin two-

dimensional (2D) materials extremely appealing for use in next-generation computing devices. While graphene, the first 2D material discovered, is a semimetal with 0 eV band gap,⁴ a class of 2D layered materials known as transition metal dichalcogenides (TMDs) have band gaps ranging from semimetallic (0 eV) to semiconducting (~ 2.5 eV) energies.^{5,6} TMDs retain sizable band gaps and carrier mobilities down to monolayer thicknesses⁷ less than 1 nm, whereas Si thinned below ~ 4 nm faces severe mobility degradation issues due to surface roughness fluctuations.^{8–10}

Specifically, MoS₂ has become one of the most promising TMDs due to its band gap (~ 2.2 eV for monolayer MoS₂^{11,12}) and controllable growth of consistent large-area MoS₂ films down to monolayer (1L) thicknesses, making MoS₂ a viable candidate for large scale semiconductor applications.^{13–18} Although moving MoS₂ away from tedious and inconsistent mechanical exfoliation techniques has enabled systematic studies for electronics applications,^{16,19,20} the quality of synthesized MoS₂ has not always been ideal, especially from the standpoint of the device fabrication thermal budget. If MoS₂ is to be integrated in the back-end (i.e. after silicon) of modern integrated circuits, the fabrication process of as-grown MoS₂ transistors cannot exceed a range of 450-to-600°C (depending on process time) for integration with logic applications.^{21–24} (Although some 3-dimensional vertical memory applications can withstand $>700^\circ\text{C}$.²⁵) For example, irreversible degradation of certain silicide contacts, inter-layer dielectrics, and diffusion barrier layers have been observed with thermal budgets over 600°C for 2 hours.^{21,26,27}

In this work, we report direct chemical vapor deposition (CVD) growth of continuous monolayer MoS₂ films using solid source precursors at 560°C in 50-minutes, within the thermal budget of modern integrated circuit processing. Comparing metrics of $I_{\text{on}}/I_{\text{off}}$ current ratio, drive current, contact resistance, and carrier mobility, transistors made from these as-grown films show performance levels similar to those reported for monolayer MoS₂ grown at higher temperatures.^{13,16,28–34} This work provides a path towards the realization of high quality, thermal-budget-compatible TMD materials for applications in transistor density scaling, to further improve new advanced computing systems.

GROWTH AND MATERIAL CHARACTERIZATION

The thermal budget for modern silicon integrated circuit processing dictates that fabrication of BEOL (back-end-of-the-line) devices and materials cannot exceed 550°C for 2 hours,^{26,27} and even more stringent temperature budgets are needed if process times are longer. This limitation is imposed by gate work function instability and silicide contact degradation.²⁷ Certain interlayer low- κ dielectrics (e.g. SiCOH) could

require even stricter thermal budgets, below 450°C for 2 hours.²¹ (Although SiCOH integrity could be maintained up to 525°C for 2 hours using some BEOL processes.²⁴) Thus, in order to incorporate new materials such as MoS₂ into stacked, heterogeneous integrated circuits that increase the transistor density in the third dimension (3D),³⁵ their BEOL thermal budget becomes crucial. However, direct, monolayer (1L) MoS₂ growths with good electrical properties have typically been obtained using solid source precursor chemical vapor deposition (CVD) above 650°C.^{13,16,28–34} Wafer-scale 1L MoS₂ grown using metal-organic CVD (MOCVD)^{14,36–41} at or below 500°C appears within the BEOL temperature budget, but the growth times have been >8 hours, which limit throughput, and the average carrier mobilities reported remain lower than the best MoS₂ grown at higher temperatures. Efforts to develop atomic layer deposition (ALD) of MoS₂ at temperatures as low as 50°C are also underway,^{42,43} but the resulting films are amorphous and require post-growth anneals above 800°C to improve their crystallinity.^{44–46}

Here, we grew continuous 1L MoS₂ films at 560°C in 50-minutes using solid sulfur (S) and molybdenum trioxide (MoO₃) precursors with the aid of perylene-3,4,9,10 tetracarboxylic acid tetrapotassium salt (PTAS).^{13,15,17,18} PTAS dissolved in water is deposited as droplets around the perimeter of 1.5 × 2 cm chips with thermally grown SiO₂ on p⁺ silicon, which also serve as back-gate for field-effect transistors.¹³ The PTAS droplets dry up into “coffee rings” around the perimeter of the substrate before the seeded SiO₂/Si chips are placed face-down on top of an alumina (Al₂O₃) crucible containing MoO₃ powder. Trace amounts of PTAS diffuse from the dried “coffee rings” towards the center of the chip to facilitate MoS₂ nucleation during growth. Excess solid sulfur source melted in a quartz boat is placed at an optimal position upstream near the incoming Ar gas flow inlet, all enclosed within a cylindrical quartz tube.

In addition to the PTAS seed layer promoting initial MoS₂ nucleation from which grains grow, the trace amounts of carbon from the diffusing seed layer also act as a catalyst, promoting reduction of MoO₃ powder into volatile suboxide MoO_{3-x}.⁴⁷ The reduction of MoO₃ into MoO_{3-x} is crucial for incoming S to react with volatile molybdenum (Mo) species in order to grow MoS₂. It is important to note that at growth temperatures around 560°C, MoO₃ reduction is near the limit of reaction with trace amounts of carbon present.⁴⁷ Both a reduced system pressure of 490 torr and incoming volatile sulfur introduced at elevated temperatures also promote the reduction of MoO₃ into volatile suboxide MoO_{3-x}.⁴⁸ When sufficient volatile MoO_{3-x} is matched with an optimal flux of incoming sulfur atoms at the substrate surface, further reaction occurs to grow 1L MoS₂ films. As shown in Figures 1a-b, relatively clean 1L MoS₂ films can be grown at 560°C in 50-minutes on 1.5 × 2 cm chips. This is the lowest thermal budget that produced clean,

sizable ($>10\ \mu\text{m}$) MoS₂ triangular grains merged into a continuous film, using solid source precursors in our system. Larger $\sim 60\ \mu\text{m}$ triangular grains are seen (a) 7 mm from the edge of the substrate, which merge into a continuous film with overlapping grain boundaries at (b) the center of the substrate.

Raman spectroscopy and photoluminescence (PL) are utilized to confirm that 1L MoS₂ is present from its characteristic phonon (lattice vibrations) and excitonic (electron-hole pair generation) properties, respectively. In order to ensure strong, well-defined detectable signals, all Raman and PL measurements were performed on 1L MoS₂ grown on 90 nm SiO₂/Si substrates using a green laser with excitation wavelength of 532 nm. Due to the Lorentzian nature of the Raman (and PL) peaks and the Gaussian nature of the laser spatial intensity, pseudo-Voigt curves were used to capture each peak fit.⁴⁹ Figure 1c shows the Raman spectrum of 1L MoS₂ grown at 560°C (blue dots). Pseudo-Voigt curves (black lines) fit the Raman peaks of 1L MoS₂, namely the in-plane E' mode at 384.5 cm⁻¹ and out-of-plane A₁' mode at 405.3 cm⁻¹ with a peak separation $\Delta f = 20.8\ \text{cm}^{-1}$, which is characteristic of as-grown 1L MoS₂^{13,50} with slight intrinsic tensile strain due to thermal coefficient of expansion (TCE) mismatch between the 2D material and the underlying SiO₂ substrate.⁵¹ Because odd-numbered, few-layer MoS₂ (including 1L MoS₂) belong to the D_{3h} point group, the two main Raman active modes are denoted E' and A₁'.^{13,52} The 2LA(M) peak is seen around 453.3 cm⁻¹ and the transverse optical (TO) shoulder peak at 378.8 cm⁻¹.⁵³

Characteristic photoluminescence (PL) measurements are shown in Figure 1d. We note these probe the optical band gap of monolayer (1L) MoS₂, which is smaller than the electronic direct band gap of 1L MoS₂ by the exciton binding energy (0.2 to 0.6 eV),¹¹ and all three of these energies depend on the environmental dielectric screening.⁵⁴ Pseudo-Voigt curves (black lines) fit the PL spectrum, identifying the ground state A exciton at 1.847 eV and the charged A⁻ trion at 1.810 eV. (The A⁻ trion is a charged exciton with an extra electron coupled to the electron-hole pair.) We did not observe a B exciton in our samples (0.1 to 0.2 eV above the A peak), which has been used to assess non-radiative recombination, with low (or no) B peak suggesting higher sample quality.⁵⁵

To further show that monolayer (1L) MoS₂ is grown by chemical vapor deposition (CVD) at 560°C, scanning electron microscopy (SEM) is shown in Figure 1e of the continuous 1L MoS₂ film at the center of the substrate with overlapping grain boundaries. Atomic force microscopy (AFM) of 1L MoS₂ triangular grains on SiO₂/Si, away from the substrate center is also shown in Figure 1f. The MoS₂ is measured to be $\sim 0.72\ \text{nm}$ thick from the step height, which is in close agreement with the accepted monolayer MoS₂ thickness (0.615 nm).⁵⁶ Growth residue (most likely caused by excess partially reduced MoO₃ precursor)

is observed on the MoS₂ grains and along the grain edges. Both SEM and AFM indicate that 1L MoS₂ is grown without bilayer (2L) MoS₂ nucleation.

ELECTRICAL RESULTS AND DISCUSSION

Transfer length method (TLM) structures⁵⁷ were fabricated on 560°C 1L MoS₂ as-grown on a 50 nm SiO₂ on p⁺ Si substrate, which also serve as the back-gate for all devices. Figure 2a shows an optical image of the TLM structures as fabricated by electron-beam lithography. The large, square probe pads (20 nm SiO₂/2 nm Ti/40 nm Au) lead into the fine contacts (70 nm Au). The colorized scanning electron microscopy (SEM) inset shows the pure Au leads directly contacting the monolayer MoS₂ channel, which was etched 18 μm long × 2 μm wide (darker region) after the contact metal deposition. Figure 2b shows the cross-section schematic of the TLM test structure with adjacent contact channel lengths ranging from $L_{\text{ch}} = 100$ nm to 700 nm, forming a series of back-gated field-effect transistors (FETs).

Figure 3a shows the measured drain current I_D (normalized by width) vs. back-gate voltage V_{GS} transfer curves at drain voltages $V_{\text{DS}} = 0.1$ V and 1 V for a 100 nm channel device ($L_{\text{ch}} = 100$ nm). The small arrows mark forward (left I_D branch) and backward (right I_D branch) voltage sweep directions, illustrating small hysteresis and charge trapping between MoS₂ and the back-gate SiO₂ dielectric. The maximum gate leakage observed was ~1 nA at $V_{\text{GS}} = 20$ V, which is 3-4 orders of magnitude smaller than the drain current in the on-state. A current ratio $I_{\text{on}}/I_{\text{off}} \sim 10^7$ is observed and the subthreshold slope (SS) is estimated $SS \approx 1150$ mV/dec from the forward sweep at $V_{\text{DS}} = 0.1$ V. We note the SS is relatively high, but can be reduced by reducing the EOT (equivalent oxide thickness) of the gate dielectric below the 50 nm SiO₂ used here. Reducing interface charge trap density at the MoS₂/dielectric interface⁵⁸ by passivating the dielectric⁵⁹ or by using a molecular crystal seeding layer⁶⁰ can also greatly improve SS when employing cleaner, dedicated fabrication outside general-purpose academic facilities.

Figure 3b shows the measured I_D vs. V_{DS} output curves at gate voltages from $V_{\text{GS}} = 5$ V to 20 V for the same $L_{\text{ch}} = 100$ nm device. The maximum drive current achieved was $I_{D,\text{max}} \sim 140$ μA/μm at $V_{\text{DS}} = 1$ V and $V_{\text{GS}} = 20$ V, which is the highest reported for monolayer MoS₂ grown below 600°C. Current saturation is not observed because the threshold voltage V_T is sufficiently negative to keep this device in the linear operating region throughout. Relatively low hysteresis is again observed from the forward and backward voltage sweeps, indicating minimal charge trapping. The measured I_D vs. V_{GS} transfer curves at $V_{\text{DS}} = 0.1$ V for channel lengths from $L_{\text{ch}} = 100$ nm to 700 nm are shown in Figure 3c. The threshold voltage V_T

ranges from 2.4 V to 5.8 V, using the linear extrapolation method.¹⁶ The measured I_D vs. V_{DS} output curves at $V_{GS} = 20$ V for channel lengths from $L_{ch} = 100$ nm to 700 nm are shown in Figure 3d. I_D decreases for increasing channel lengths as expected, due to larger channel resistance contribution, for a constant V_{DS} and constant contact resistance (R_C).

We next turn to estimating contact resistance (R_C) first and then the carrier mobility from TLM structures. In addition to a better estimation of R_C , the MoS₂ channel sheet resistance (R_{sh}) can also be accurately extracted from the slope of the linear TLM extrapolation. The sheet resistance is then used to estimate the effective mobility, $\mu_{eff} = (qnR_{sh})^{-1}$ where q is the elementary charge and n is the carrier concentration. Here $n = C_{ox}(V_{GS} - V_T - V_{DS}/2)/q$ as all our transistors remain in the linear regime, where C_{ox} is the gate dielectric capacitance per unit area (~ 70 nF/cm² for our 50 nm SiO₂). We note V_T must be individually assessed for each channel in the TLM to account for any device-to-device variation.

Figure 4a shows the linear TLM fit of total measured resistance ($R_{tot} = R_{sh} + 2R_C$, normalized by width) vs. channel length (L_{ch}) extracted from Figure 3d at a carrier concentration $n = 6.1 \times 10^{12}$ cm⁻² (at the same gate overdrive, $V_{OV} = V_{GS} - V_T = 14$ V, not the same gate voltage V_{GS}). The V_T is extracted for each channel length in Figure 3c by the linear extrapolation method.^{57,61} The y -intercept of the linear fit in Figure 4a corresponds to the total contact resistance, $2R_C$. We note that it is important to perform such TLM fits using a wide range of channel lengths (from short, R_C -dominated to long, R_{sh} -dominated) in order to minimize the R_C extrapolation error. The remaining uncertainty of the linear TLM fit represents the intrinsic device-to-device variation. Figure 4b shows the effective mobility (μ_{eff}) as a function of carrier concentration n , obtained from the sheet resistance slope of the TLM plot. At $n = 6.1 \times 10^{12}$ cm⁻², the effective carrier mobility is $\mu_{eff} = 29 \pm 5$ cm²V⁻¹s⁻¹, which is comparable to the mobilities reported at higher growth temperatures.^{13,16,28-31,33,34} Figure 4c shows the contact resistance (R_C , normalized by width) also as a function of carrier concentration n . The contact resistance was $R_C = 4.9 \pm 1.3$ k Ω · μ m at $n = 6.1 \times 10^{12}$ cm⁻² with the error bound corresponding to the 95% confidence interval of the line fits.

In Figure 5 we compare the room temperature electron mobility data of our films grown at 560°C with previous reports, for other CVD-grown (and MOCVD-grown³⁶⁻⁴¹) 1L MoS₂ reported in the literature,^{13,16,63-67,18,20,28-30,32,34,62} as a function of growth temperature (up to 900°C). We note some reports are given as effective mobility^{13,16,28-30} (μ_{eff} from TLM, denoted by squares), others are only available as field-effect mobility^{18,20,67,32,34,36,62-66} (μ_{FE} , denoted by triangles). The effective mobility values from this work (grown at 560°C for 50-minutes) are marked in yellow. The field-effect mobility values reported from

MOCVD growths (at or below 500°C for 8 to 30 hours) are marked in blue.³⁶⁻⁴¹ For this simple comparison we benchmark two-probe mobility measurements, although more complex four-probe measurements with a threshold voltage correction can yield more accurate mobility values,⁶⁸ if current shunt paths through the (invasive) inner voltage probes are avoided.⁷ In general, we have found no correlation between carrier mobility and growth temperature, only between growth temperature and MoS₂ crystallite size or substrate adhesion. Growth times (at maximum process temperature) are also labeled, indicating significantly longer growths reported for MOCVD to attain full coverage 1L MoS₂.

First, comparing the effective 1L MoS₂ mobilities (μ_{eff} , squares), we observe that our values (29 and 33 cm²V⁻¹s⁻¹ from 560°C growths at a reduced 490 torr pressure) are similar to the μ_{eff} from MoS₂ grown at higher temperatures, up to 850°C.^{13,16,28-30} (Recent simulations have shown mobilities in this range are limited by point defects, most likely charge impurities and sulfur vacancies.^{69,70}) Field-effect mobility (μ_{FE}) data reported for 1L MoS₂ grown at 850°C (lighter hollow triangles) are also included as a box-and-whisker plot (average μ_{FE} of 34.2 cm²V⁻¹s⁻¹ outlined in the black box)¹⁶ in good agreement with the 850°C effective mobility. For CVD-grown 1L MoS₂ using solid source precursors, our values are the highest reported mobilities to date with a thermal budget below 2-hours at 600°C. One notable difference is that our past 850°C growths have yielded up to ~10% bilayer regions,¹⁶ while such bilayer regions are undiscernible on the 560°C growths presented here (Figure 1). In addition, we have also found the MoS₂ grown at 560°C to be more weakly adhered to the SiO₂ substrate compared to our previous studies at higher growth temperatures,^{13,16,28-30} which necessitated careful electron-beam lithography without exposing the MoS₂ samples to water, to avoid delamination during processing.^{71,72} We note that adhesion challenges, in addition to the growth residue observed on the 1L MoS₂ grains and along the grain edges, could have also led to some of our observed device-to-device variation.

When comparing effective mobility values with field-effect mobilities (μ_{FE} , triangles) reported across the literature, most μ_{FE} reported are lower. This is mainly due to the effects of contact resistance, although material quality, non-ideal contact selection and device fabrication (in academic facilities) could also cause the large μ_{FE} variation observed, with no clear trends between studies and across growth temperatures. It is also possible that μ_{FE} is overestimated in some studies, depending on the gate-voltage-dependence of the contacts. In other words, a sharp turn-on of back-gated contacts can lead to an overestimated peak transconductance g_{m} and μ_{FE} .^{68,73,74} Due to these effects of gated contacts, effective mobility (μ_{eff})

from sheet resistance (TLM) measurements (particularly when reported as a function of carrier density n) tend to be more reliable and are preferable rather than μ_{FE} , as the main figure of merit for MoS₂.

CONCLUSIONS

We have demonstrated direct CVD solid source precursor growth of monolayer (1L) MoS₂ at 560°C in 50-minutes, with electrical and optical properties very similar to those of CVD MoS₂ grown at higher temperatures. Our films are within the 450-to-600°C, 2-hour thermal budget window required for back-end-of-the-line (BEOL) compatibility with modern silicon integrated circuit processing. These new 1L MoS₂ films growths were enabled by carefully matching an optimized sulfur flux to sufficient volatile MoO_{3-x} reduced in the presence of the carbon-based PTAS seed layer. Electrical measurements revealed a maximum drive current $I_{D,max} \sim 140 \mu A/\mu m$, which is the highest reported for 1L MoS₂ grown below 600°C using solid source precursors. The effective electron mobility was extracted with transfer length method (TLM) test structures as $\mu_{eff} = 29 \pm 5 \text{ cm}^2\text{V}^{-1}\text{s}^{-1}$ at a carrier concentration of $6.1 \times 10^{12} \text{ cm}^{-2}$, which is comparable to mobilities reported from films grown at higher temperatures. The results of this work provide a path towards the realization of high quality, thermal-budget-compatible TMDs for heterogeneous integration with silicon manufacturing. These could enable 3D integration of such 2D materials for advanced functionalities in memory or power-gating circuits (with low-leakage BEOL transistors) or high-density logic, in the third dimension.

METHODS

560°C 1L MoS₂ Chemical Vapor Deposition Growth

PTAS (perylene-3,4,9,10 tetracarboxylic acid tetrapotassium salt) dissolved in water was deposited as droplets around the perimeter of $1.5 \times 2 \text{ cm}$ chips of thermally grown 50 nm SiO₂ on p⁺ silicon that were initially rinsed with de-ionized (DI) water.¹³ The PTAS droplets dry up into “coffee rings” around the perimeter of the substrate before the seeded SiO₂/Si chips were placed face-down on top of an alumina (Al₂O₃) crucible containing ~2 mg of MoO₃ powder (Alfa Aesar, Puratronic 99.9995% purity) spread into a ~1 cm diameter circle. ~100 mg of excess solid sulfur source (Alfa Aesar, Puratronic 99.999% purity) melted in a quartz boat was placed ~26 cm away from the center near the incoming Ar gas flow inlet, all enclosed within a 55 mm inner diameter quartz tube. Before each growth, the system was flushed for 5

minutes using 1500 sccm Ar gas under vacuum before setting the ambient condition to 490 torr at 22 sccm Ar flow rate, adjusting the throttle valve. For the growth temperature cycle, the tube furnace was first ramped from room temperature to 450°C in 10 minutes and then subsequently ramped to 560°C in 5 minutes. The temperature was held at 560°C for 50 minutes before rapidly cooling down to room temperature by opening the furnace hatch. The partially reduced MoO₃ source must be cleaned out and replenished after each growth cycle, while the excess solid sulfur source can be re-used in subsequent growths.

MoS₂ Device Fabrication

Contact probe pads and coarse contacts were defined by e-beam lithography using a bilayer resist stack of 250 nm MMA/50 nm PMMA. This promotes resist undercutting for easier contact metal liftoff which helps maintain MoS₂ adhesion to the growth substrate. This was followed by e-beam evaporation of 20 nm SiO₂/2 nm Ti/70 nm Au, all layers deposited at 0.5 Å/s at a base-pressure of 10⁻⁷ torr. The 20 nm SiO₂ layer helps mitigate pad-to-gate leakage through the back-gate dielectric. This was followed by an overnight lift-off in acetone at room temperature. Fine contacts were patterned using e-beam lithography with a 60 nm PMMA 495K/215 nm PMMA 950K bilayer resist-stack which provides fine resolution along with sufficient undercutting for effective liftoff. 70 nm Au was then deposited by e-beam evaporation at a deposition rate of 0.5 Å/s at a base pressure below 10⁻⁷ torr without any adhesion layer to achieve a clean contact interface. The liftoff was carried out in Remover PG solvent for 30 minutes at 80°C. MoS₂ was patterned into uniform rectangular channels of 2 μm width by photolithography followed by a gentle O₂ plasma etch. The O₂ plasma etch was carried out at a power of 10 W in a chamber set to 20 mTorr pressure and 20 sccm O₂ flow rate for 60 seconds. All electrical measurements were carried out at room temperature in a vacuum probe station at ~10⁻⁵ torr after an in-situ vacuum anneal at 250°C for 2 hours.

Optical, Electrical, and AFM Characterization

Raman and PL data were taken using a Horiba Labram with a 532 nm excitation laser. All electrical measurements were performed in the dark and under vacuum (<10⁻⁵ Torr) using a Keithley 4200-SCS parameter analyzer, in a Janis ST-100 probe station, at room temperature. Scanning electron microscopy (SEM) was conducted using a Thermo Fisher Scientific Apreo S SEM equipped with a NiCol electron column operated in immersion mode. Atomic force microscopy (AFM) was conducted using a Bruker Dimension Icon AFM system operated in tapping mode.

AUTHOR INFORMATION

Corresponding Author: *E-mail: epop@stanford.edu

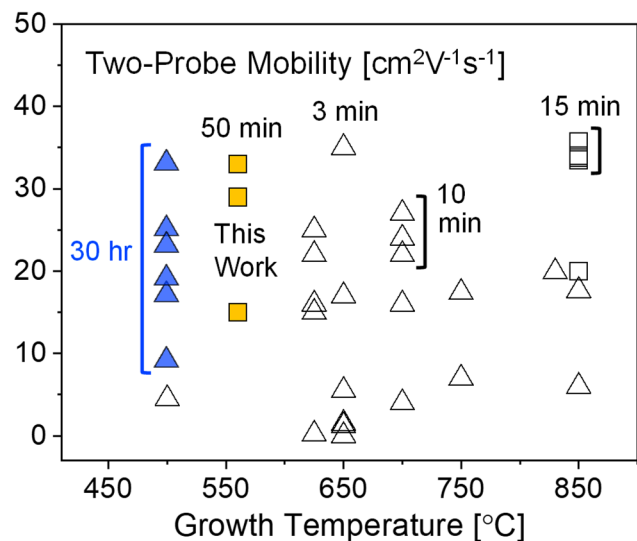
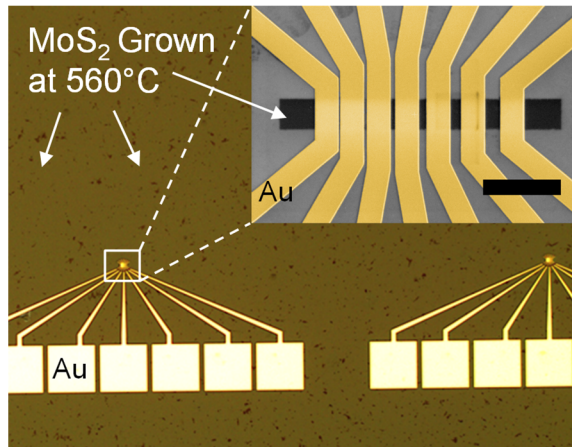
Author Contributions: A.T., A.K., and E.P. conceived the experiments and wrote the manuscript with input from all authors. A.T. grew the MoS₂ and performed the Raman and PL characterization. A.K. and M.J. performed the SEM and AFM characterization respectively. A.K., M.J., and A.T. fabricated the devices. A.K. and A.T. performed the electrical measurements and data analysis.

Competing Interests: The authors declare that they have no competing interests.

ACKNOWLEDGEMENTS

This work was supported in part by ASCENT, one of six centers in JUMP, a Semiconductor Research Corporation (SRC) program sponsored by DARPA; the National Science Foundation (NSF) EFRI 2-DARE Award 1542883; and member companies of the Advanced Materials Enabling Novel Devices (AMEND) focus area of the Stanford SystemX Alliance, an industrial affiliate program at Stanford University. Work was performed in part at the Stanford Nanofabrication Facility (SNF) and the Stanford Nano Shared Facilities (SNSF), which received funding from the National Science Foundation (NSF) as part of National Nanotechnology Coordinated Infrastructure Award ECCS-1542152.

TABLE OF CONTENTS GRAPHIC



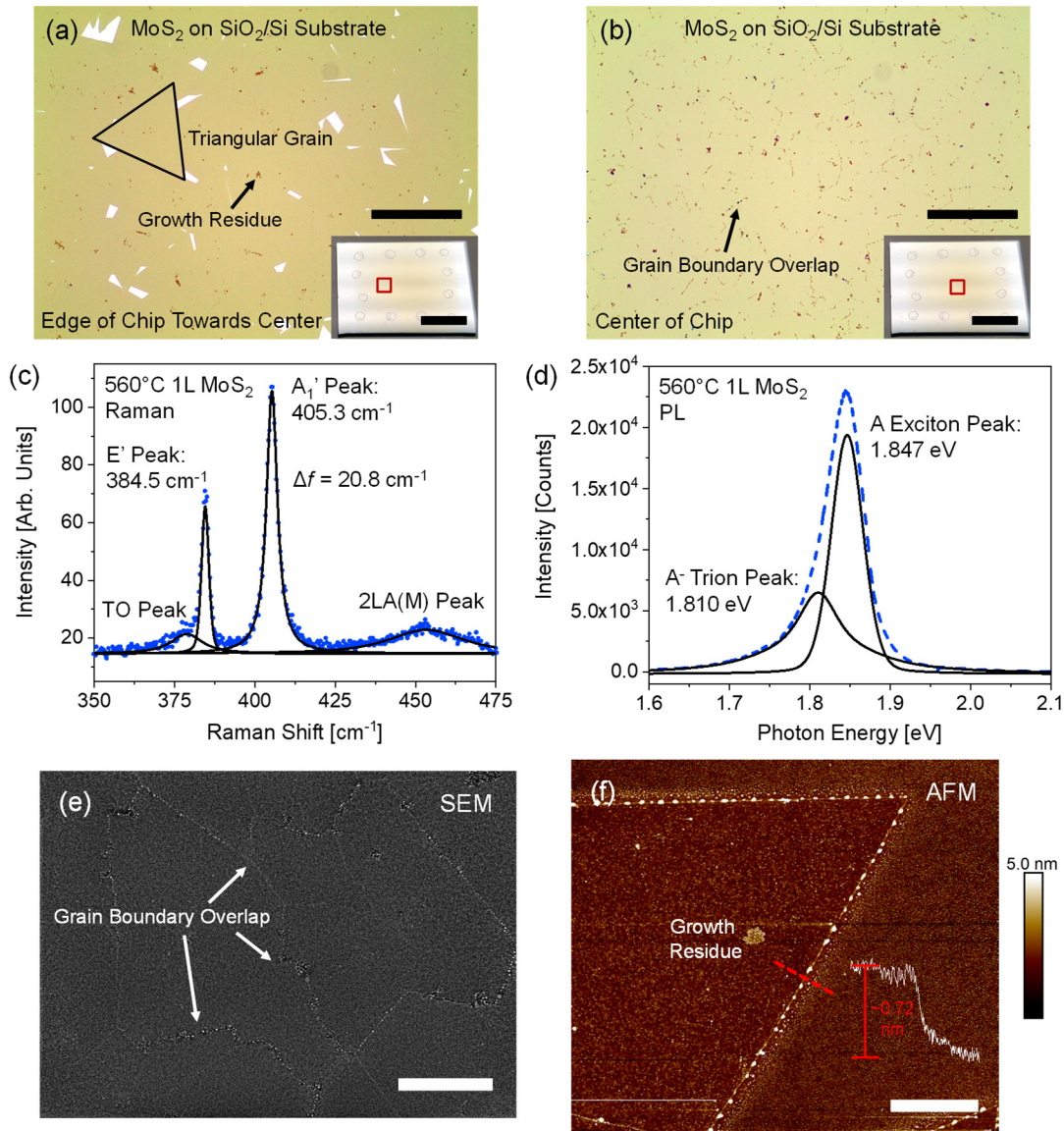


Figure 1. Monolayer MoS₂ grown at 560°C. (a, b) Optical images of monolayer (1L) MoS₂ grown by chemical vapor deposition (CVD) at 560°C on SiO₂/Si at (a) 7 mm from edge of the substrate; (b) center of the substrate. Larger ~60 μm triangular grains are seen 7 mm from the edge, which merge into a continuous film with overlapping grain boundaries at the center. Optical image scale bars are 20 μm. Insets show the 1.5 × 2 cm substrates, with red boxes marking the location of the optical images. Circles are “coffee rings” corresponding to the PTAS droplets. Inset scale bars are 7 mm. (c) Raman spectrum of 1L MoS₂ grown at 560°C on SiO₂/Si (blue dots). Pseudo-Voigt curves (black lines) fit the E' mode at 384.5 cm⁻¹ and the A₁' mode at 405.3 cm⁻¹ with a peak separation Δf = 20.8 cm⁻¹. The longitudinal acoustic 2LA(M) peak is centered at 453.3 cm⁻¹ and the transverse optical (TO) shoulder peak is centered at 378.8 cm⁻¹. (d) Photoluminescence (PL) spectrum of the same 1L MoS₂ (blue dashed line). Pseudo-Voigt curves (black lines) fit the A exciton peak at 1.847 eV and the charged A⁻ trion peak at 1.810 eV. A laser with an excitation wavelength of 532 nm was used for all Raman and PL measurements. (e) Scanning electron

microscopy (SEM) of the continuous 1L MoS₂ film at the center of the substrate with overlapping grain boundaries. Scale bar is 3 μm. (f) Atomic force microscopy (AFM) of 1L MoS₂ triangular grains on SiO₂/Si, away from the substrate center. The MoS₂ is measured to be ~0.72 nm thick from the step height, which is in close agreement with the accepted monolayer MoS₂ thickness (0.615 nm).⁵⁶ Growth residue (most likely caused by excess partially reduced MoO₃ precursor) is observed on the MoS₂ grains and along the grain edges. Scale bar is 2 μm. Both SEM and AFM indicate that 1L MoS₂ is grown without bilayer (2L) MoS₂ nucleation.

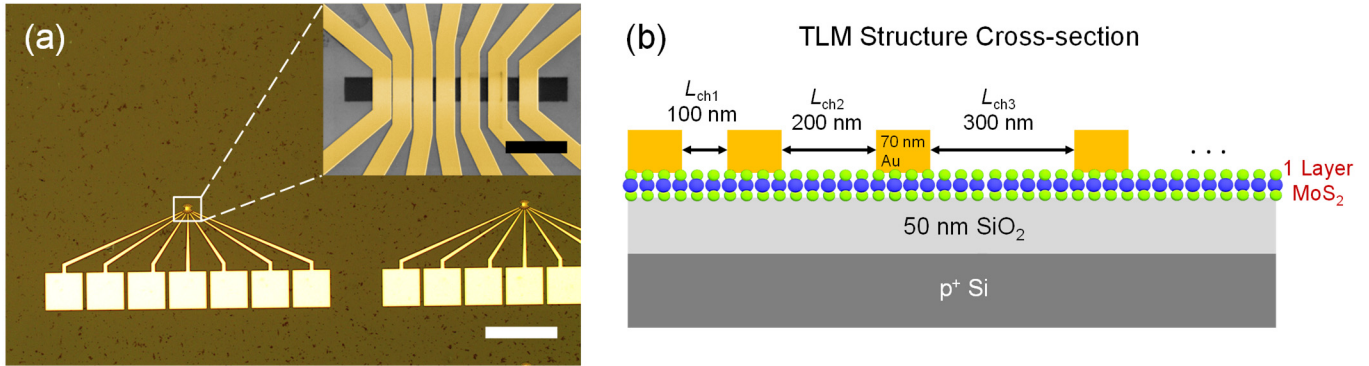


Figure 2. Transfer length method (TLM) structures. (a) Optical image of the TLM structures with channels ranging from $L_{ch} = 100$ nm to 700 nm. The large, square probe pads (20 nm SiO₂/2 nm Ti/40 nm Au) lead into the fine contacts (70 nm Au). Scale bar is 100 μ m. Inset: Enlarged, colorized scanning electron microscopy (SEM) of the fine leads directly contacting the monolayer MoS₂ channel. The channel was etched 18 μ m long \times 2 μ m wide (darker region) after the contact metal deposition. Inset scale bar is 5 μ m. (b) Cross-section schematic of the TLM test structure. The gold contact lengths are 1.5 μ m wide (not to scale). The Si substrate serves as the gate (G) and pairs of Au contacts as the drain (D) and grounded source (S) in subsequent measurements.

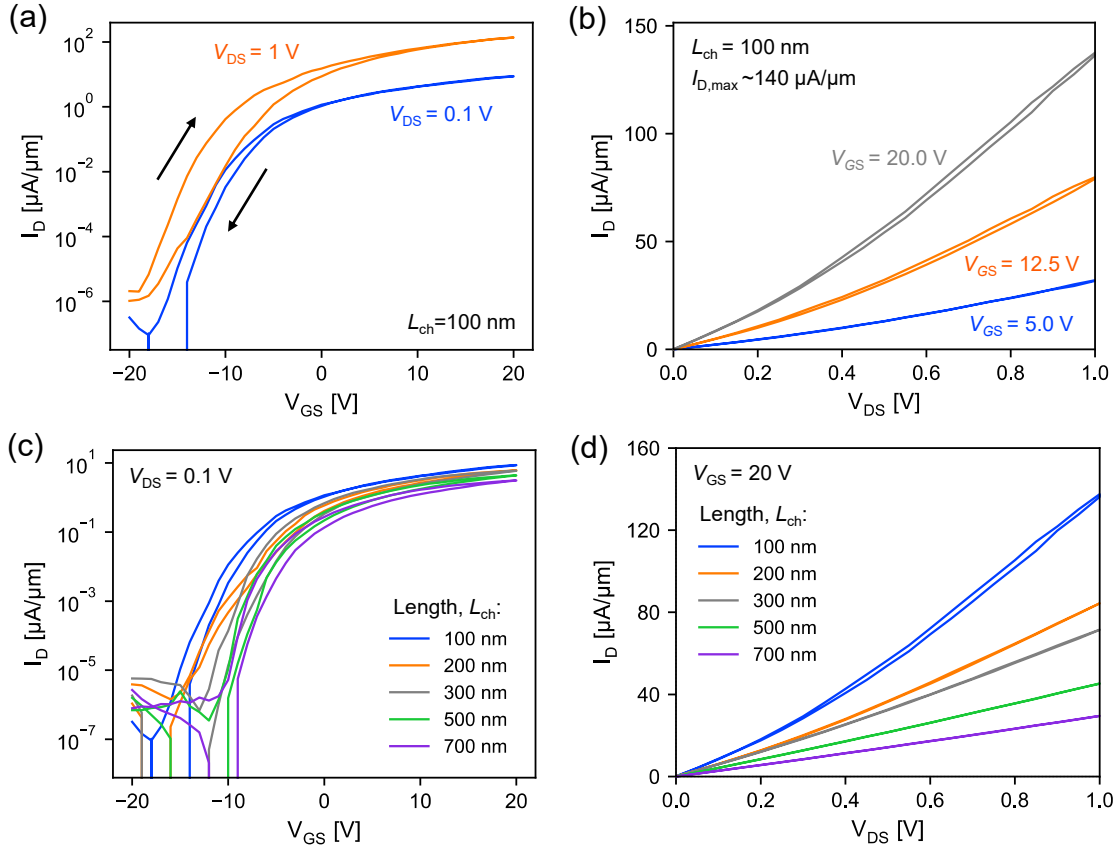


Figure 3. Electrical characteristics. Transistors fabricated using monolayer MoS₂ grown at 560°C on SiO₂/Si substrates. (a) Measured I_D vs. V_{GS} transfer curves at $V_{DS} = 0.1$ V and 1 V for a 100 nm channel device ($L_{ch} = 100$ nm). The small arrows mark forward (left I_D branch) and backward (right I_D branch) voltage sweep directions, illustrating small hysteresis. A current ratio $I_{on}/I_{off} \sim 10^7$ is observed and the subthreshold slope is estimated to be $SS \approx 1150$ mV/dec from the forward sweep at $V_{DS} = 0.1$ V. (b) Measured I_D vs. V_{DS} curves at $V_{GS} = 5$ V to 20 V for the same $L_{ch} = 100$ nm channel length device. The maximum drive current achieved was $I_{D,max} \sim 140 \mu\text{A}/\mu\text{m}$ at $V_{DS} = 1$ V. Current saturation was not observed because the threshold voltage V_T is sufficiently negative to keep this device in the linear operating region throughout.³⁰ (c) Measured I_D vs. V_{GS} transfer curves at $V_{DS} = 0.1$ V for transistors with channel lengths from $L_{ch} = 100$ nm to 700 nm. A negative threshold voltage ($V_T < 0$) is observed for all devices in this report. (d) Measured I_D vs. V_{DS} at $V_{GS} = 20$ V for transistors with channel lengths from $L_{ch} = 100$ nm to 700 nm. I_D decreases for increasing channel lengths as expected, due to larger channel resistance. All device channels are 2 μm wide and all measurements were performed at room temperature in a vacuum probe station. All electrical measurements shown are double-sweeps (voltage swept up and down), revealing minimal hysteresis.

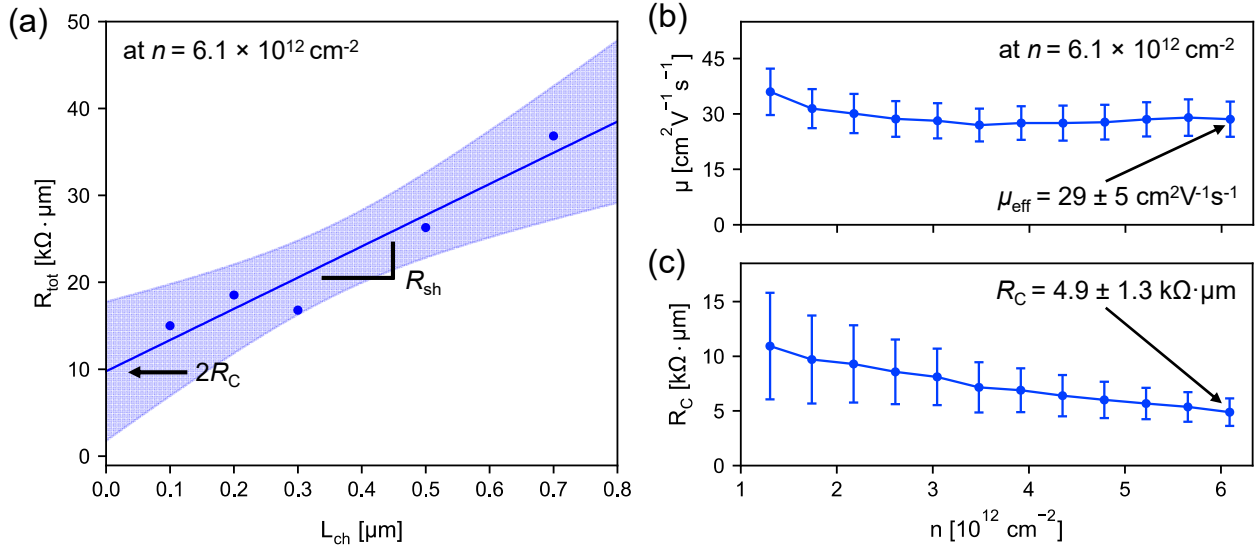


Figure 4. Sheet resistance and mobility. (a) Linear TLM fit of the total measured resistance (R_{tot} , normalized by width) as a function of channel length (L_{ch}) at a carrier concentration $n = 6.1 \times 10^{12} \text{ cm}^{-2}$, corresponding to the same gate overdrive, $V_{\text{OV}} = V_{\text{GS}} - V_{\text{T}} = 14 \text{ V}$. The y-intercept corresponds to twice the contact resistance ($2R_C$) while the slope of the line is the sheet resistance (R_{sh}). The shaded region marks the 95% confidence bound of the line fit. (b) Effective mobility (μ_{eff}) vs. n as obtained from the sheet resistance. Here, $\mu_{\text{eff}} = 29 \pm 5 \text{ cm}^2 \text{ V}^{-1} \text{ s}^{-1}$ at $n = 6.1 \times 10^{12} \text{ cm}^{-2}$, which is comparable to previous reports of monolayer MoS₂ grown at higher temperatures (see Figure 5). (c) Contact resistance (R_C , normalized by width) as a function of carrier concentration, n . The contact resistance was down to $R_C = 4.9 \pm 1.3 \text{ k}\Omega \cdot \mu\text{m}$ at $n = 6.1 \times 10^{12} \text{ cm}^{-2}$. All measurements were taken at $V_{\text{DS}} = 0.1 \text{ V}$ and room temperature in a vacuum probe station.

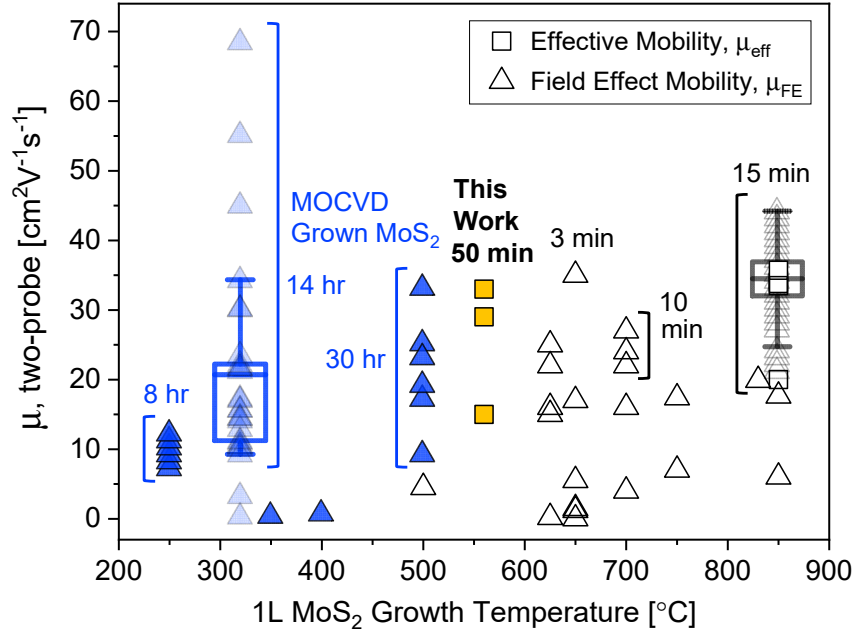


Figure 5. Monolayer MoS₂ electron mobility vs. growth temperature. Reported effective mobilities (μ_{eff} from TLM) are squares and two-probe field-effect mobilities (μ_{FE}) are triangles. The μ_{eff} from this report are marked in yellow. Metal-organic chemical vapor deposition (MOCVD) data^{36–41} are μ_{FE} marked in blue and solid-source CVD data from the literature^{13,16,63–67,18,20,28–30,32,34,62} are hollow symbols. Growth times (at maximum process temperature) are also labeled, indicating significantly longer growths reported for MOCVD to attain full coverage 1L MoS₂. The CVD films in this work were grown at 560°C for 50-minutes, while MOCVD films were grown at or below 500°C for 8 to 30 hours,^{36–41} as labeled. The μ_{eff} from sheet resistance (TLM) measurements tend to be more reliable, while μ_{FE} could be under- or over-estimated depending on the V_{GS} -dependence of gated contacts.^{68,73,74} All mobility data reported at room temperature. During review, we became aware of recent MOCVD films grown at 320°C for over 14 hours;^{37,38} a summary of μ_{FE} data for these films (lighter blue triangles) is shown as the box-and-whisker plot at 320°C (average μ_{FE} of 20.4 cm²V⁻¹s⁻¹ outlined in the blue box).

REFERENCES

1. Wong, H. S. P. *et al.* A Density Metric for Semiconductor Technology. *Proc. IEEE* **108**, 478–482 (2020).
2. Bae, G. *et al.* 3nm GAA Technology Featuring Multi-Bridge-Channel FET for Low Power and High Performance Applications. in *Technical Digest - International Electron Devices Meeting, IEDM 28.7.1-28.7.4* (IEEE, 2018). doi:10.1109/IEDM.2018.8614629.
3. Yan, R. H., Ourmazd, A. & Lee, K. F. Scaling the Si MOSFET: From Bulk to SOI to Bulk. *IEEE Trans. Electron Devices* **39**, 1704–1710 (1992).
4. K. S. Novoselov, A. K. Geim, S. V. Morozov, D. Jiang, Y. Zhang, S. V. Dubonos, I. V. G. and A. A. F. Electric Field Effect in Atomically Thin Carbon Films. **306**, 666–669 (2016).
5. Schulman, D. S., Arnold, A. J. & Das, S. Contact Engineering for 2D Materials and Devices. *Chem. Soc. Rev.* **47**, 3037–3058 (2018).
6. Shen, P. C. *et al.* CVD Technology for 2-D Materials. *IEEE Trans. Electron Devices* **65**, 4040–4052 (2018).
7. English, C. D., Shine, G., Dorgan, V. E., Saraswat, K. C. & Pop, E. Improved Contacts to MoS₂ Transistors by Ultra-high Vacuum Metal Deposition. *Nano Lett.* **16**, 3824–3830 (2016).
8. Uchida, K., Watanabe, H., Koga, J., Kinoshita, A. & Takagi, S. Experimental Study on Carrier Transport Mechanism in Ultrathin-body SOI MOSFETs n- and p-MOSFETs with SOI Thickness less than 5 nm. in *Technical Digest - International Electron Devices Meeting, IEDM 2.7.1-2.7.4* (IEEE, 2002). doi:10.1109/IEDM.2002.1175776.
9. Uchida, K., Koga, J. & Takagi, S. Experimental Study on Carrier Transport Mechanisms in Double- and Single-Gate Ultrathin-Body MOSFETs - Coulomb Scattering, Volume Inversion, and δT SOI-induced Scattering. in *Technical Digest - International Electron Devices Meeting, IEDM 33.5.1-33.5.4* (IEEE, 2003). doi:10.1109/IEDM.2003.1269402.
10. Schmidt, M. *et al.* Mobility Extraction in SOI MOSFETs with Sub 1 nm Body Thickness. *Solid. State. Electron.* **53**, 1246–1251 (2009).
11. Zhang, C., Johnson, A., Hsu, C. L., Li, L. J. & Shih, C. K. Direct Imaging of Band Profile in Single Layer MoS₂ on Graphite: Quasiparticle Energy Gap, Metallic Edge States, and Edge Band Bending. *Nano Lett.* **14**, 2443–2447 (2014).
12. Hill, H. M., Rigosi, A. F., Rim, K. T., Flynn, G. W. & Heinz, T. F. Band Alignment in MoS₂/WS₂ Transition Metal Dichalcogenide Heterostructures Probed by Scanning Tunneling Microscopy and Spectroscopy. *Nano Lett.* **16**, 4831–4837 (2016).
13. Smithe, K. K. H., English, C. D., Suryavanshi, S. V & Pop, E. Intrinsic Electrical Transport and Performance Projections of Synthetic Monolayer MoS₂ Devices. *2D Mater.* **4**, 011009 (2017).
14. Kang, K. *et al.* High-mobility Three-atom-thick Semiconducting Films with Wafer-scale Homogeneity. *Nature* **520**, 656–660 (2015).
15. Ling, X. *et al.* Role of the Seeding Promoter in MoS₂ Growth by Chemical Vapor Deposition. *Nano Lett.* **14**, 464–472 (2014).
16. Smithe, K. K. H., Suryavanshi, S. V., Muñoz Rojo, M., Tedjarati, A. D. & Pop, E. Low Variability in Synthetic Monolayer MoS₂ Devices. *ACS Nano* **11**, 8456–8463 (2017).
17. Lee, Y. H. *et al.* Synthesis and Transfer of Single-layer Transition Metal Disulfides on Diverse Surfaces. *Nano Lett.* **13**, 1852–1857 (2013).
18. Lee, Y. H. *et al.* Synthesis of Large-area MoS₂ Atomic Layers with Chemical Vapor Deposition. *Adv. Mater.* **24**, 2320–2325 (2012).
19. Wang, H. *et al.* Integrated Circuits Based on Bilayer MoS₂ Transistors. *Nano Lett.* **12**, 4674–4680 (2012).
20. Yu, L. *et al.* Graphene/MoS₂ Hybrid Technology for Large-scale Two-dimensional Electronics. *Nano Lett.* **14**, 3055–3063 (2014).
21. Deprat, F. *et al.* Dielectrics Stability for Intermediate BEOL in 3D Sequential Integration. *Microelectron. Eng.* **167**, 90–94 (2017).
22. Fenouillet-Beranger, C. *et al.* Guidelines for Intermediate Back End of Line (BEOL) for 3D Sequential Integration. in *European Solid-State Device Research Conference 252–255* (IEEE, 2017). doi:10.1109/ESSDERC.2017.8066639.
23. Schmitz, J. Low Temperature Thin Films for Next-generation Microelectronics (Invited). *Surf. Coatings*

- Technol.* **343**, 83–88 (2018).
24. Fenouillet-Beranger, C. *et al.* A Review of Low Temperature Process Modules Leading Up to the First ($\leq 500^\circ\text{C}$) Planar FDSOI CMOS Devices for 3-D Sequential Integration. *IEEE Trans. Electron Devices* **68**, 3142–3148 (2021).
 25. Lisoni, J. G. *et al.* Laser Thermal Anneal of Polysilicon Channel to Boost 3D Memory Performance. *Dig. Tech. Pap. - Symp. VLSI Technol.* (2014) doi:10.1109/VLSIT.2014.6894346.
 26. Fenouillet-Beranger, C. *et al.* FDSOI Bottom MOSFETs Stability versus Top Transistor Thermal Budget Featuring 3D Monolithic Integration. in *European Solid-State Device Research Conference* vol. September 110–113 (IEEE, 2014).
 27. Fenouillet-Beranger, C. *et al.* New Insights on Bottom Layer Thermal Stability and Laser Annealing Promises for High Performance 3D VLSI. in *Technical Digest - International Electron Devices Meeting, IEDM 27.5.1-27.5.4* (IEEE, 2014). doi:10.1109/IEDM.2014.7047121.
 28. English, C. D., Smithe, K. K. H., Xu, R. L. & Pop, E. Approaching Ballistic Transport in Monolayer MoS₂ Transistors with Self-aligned 10 nm Top Gates. in *Technical Digest - International Electron Devices Meeting, IEDM 5.6.1-5.6.4* (IEEE, 2017). doi:10.1109/IEDM.2016.7838355.
 29. McClellan, C. J., Yalon, E., Smithe, K. K. H., Suryavanshi, S. V. & Pop, E. High Current Density in Monolayer MoS₂ Doped by AlO_x. *ACS Nano* **15**, 1587–1596 (2021).
 30. Smithe, K. K. H., English, C. D., Suryavanshi, S. V. & Pop, E. High-Field Transport and Velocity Saturation in Synthetic Monolayer MoS₂. *Nano Lett.* **18**, 4516–4522 (2018).
 31. Sanne, A. *et al.* Radio Frequency Transistors and Circuits Based on CVD MoS₂. *Nano Lett.* **15**, 5039–5045 (2015).
 32. Wang, Y. *et al.* Van der Waals Contacts between Three-Dimensional Metals and Two-dimensional Semiconductors. *Nature* **568**, 70–74 (2019).
 33. Leong, W. S. *et al.* Synthetic Lateral Metal-Semiconductor Heterostructures of Transition Metal Disulfides. *J. Am. Chem. Soc.* **140**, 12354–12358 (2018).
 34. Dumcenco, D. *et al.* Large-area Epitaxial Monolayer MoS₂. *ACS Nano* **9**, 4611–4620 (2015).
 35. Aly, M. M. S. *et al.* Energy-efficient Abundant-data Computing: The N3XT 1,000. *Computer (Long Beach, Calif.)* **48**, 24–33 (2015).
 36. Guimarães, M. H. D. *et al.* Atomically Thin Ohmic Edge Contacts between Two-Dimensional Materials. *ACS Nano* **10**, 6392–6399 (2016).
 37. Shen, P.-C. *et al.* Ultralow Contact Resistance between Semimetal and Monolayer Semiconductors. *Nature* **593**, 211–217 (2021).
 38. Park, J. *et al.* Synthesis of High-Performance Monolayer Molybdenum Disulfide at Low Temperature. *Small Methods* **5**, 2000720 (2021).
 39. Mun, J. *et al.* Low-temperature Growth of Layered Molybdenum Disulphide with Controlled Clusters. *Sci. Rep.* **6**, 21854 (2016).
 40. Mun, J. *et al.* High-Mobility MoS₂ Directly Grown on Polymer Substrate with Kinetics-controlled Metal-organic Chemical Vapor Deposition. *ACS Appl. Electron. Mater.* **1**, 608–616 (2019).
 41. Kim, T. *et al.* Wafer-scale Production of Highly Uniform Two-dimensional MoS₂ by Metal-organic Chemical Vapor Deposition. *Nanotechnology* **28**, 18LT01 (2017).
 42. Cai, J., Han, X., Wang, X. & Meng, X. Atomic Layer Deposition of Two-dimensional Layered Materials: Processes, Growth Mechanisms, and Characteristics. *Matter* **2**, 587–630 (2020).
 43. Huang, Y. & Liu, L. Recent Progress in Atomic Layer Deposition of Molybdenum Disulfide: A Mini Review. *Sci. China Mater.* **62**, 913–924 (2019).
 44. Tan, L. K. *et al.* Atomic Layer Deposition of a MoS₂ Film. *Nanoscale* **6**, 10584–10588 (2014).
 45. Jurca, T. *et al.* Low-Temperature Atomic Layer Deposition of MoS₂ Films. *Angew. Chemie - Int. Ed.* **56**, 4991–4995 (2017).
 46. Cadot, S. *et al.* A Novel 2-step ALD Route to Ultra-thin MoS₂ Films on SiO₂ through a Surface Organometallic Intermediate. *Nanoscale* **9**, 538–546 (2017).
 47. Zhang, G. H., Wang, D. H., Wang, L., Chou, K. C. & Dong, A. Preparation of Industrial Grade MoO₂ by the Reaction between Industrial Grade MoO₃ and Activated Carbon. *Metall. Res. Technol.* **115**, 416 (2018).

48. Li, X. L. & Li, Y. D. Formation of MoS₂ Inorganic Fullerenes (IFs) by the Reaction of MoO₃ Nanobelts And S. *Chem. - A Eur. J.* **9**, 2726–2731 (2003).
49. Verhagen, T., Guerra, V. L. P., Haider, G., Kalbac, M. & Vejpravova, J. Towards the Evaluation of Defects in MoS₂ using Cryogenic Photoluminescence Spectroscopy. *Nanoscale* **12**, 3019–3028 (2020).
50. Schauble, K. *et al.* Uncovering the Effects of Metal Contacts on Monolayer MoS₂. *ACS Nano* **14**, 14798–14808 (2020).
51. Ahn, G. H. *et al.* Strain-engineered Growth of Two-dimensional Materials. *Nat. Commun.* **8**, 1–7 (2017).
52. Molina-Sánchez, A. & Wirtz, L. Phonons in Single-layer and Few-layer MoS₂ and WS₂. *Phys. Rev. B - Condens. Matter Mater. Phys.* **84**, 155413 (2011).
53. Shi, W. *et al.* Phonon Confinement Effect in Two-dimensional Nanocrystallites of Monolayer MoS₂ to Probe Phonon Dispersion Trends Away from Brillouin-Zone Center. *Chinese Phys. Lett.* **33**, 057801 (2016).
54. Ryou, J., Kim, Y. S., Santosh, K. C. & Cho, K. Monolayer MoS₂ Bandgap Modulation by Dielectric Environments and Tunable Bandgap Transistors. *Sci. Rep.* **6**, 29184 (2016).
55. McCreary, K. M., Hanbicki, A. T., Sivaram, S. V. & Jonker, B. T. A- and B-exciton Photoluminescence Intensity Ratio as a Measure of Sample Quality for Transition Metal Dichalcogenide Monolayers. *APL Mater.* **6**, 111106 (2018).
56. Dickinson, R. G. & Pauling, L. The Crystal Structure of Molybdenite. *J. Am. Chem. Soc.* **45**, 1466–1471 (1923).
57. Schroder, D. K. *Semiconductor Material and Device Characterization*. (John Wiley & Sons, Inc., 2006). doi:10.1002/0471749095.
58. Illarionov, Y. Y. *et al.* Insulators for 2D Nanoelectronics: The Gap to Bridge. *Nat. Commun.* **11**, 3385 (2020).
59. Bolshakov, P. *et al.* Improvement in Top-gate MoS₂ Transistor Performance due to High Quality Backside Al₂O₃ Layer. *Appl. Phys. Lett.* **111**, 032110 (2017).
60. Li, W. *et al.* Uniform and Ultrathin High-κ Gate Dielectrics for Two-dimensional Electronic Devices. *Nat. Electron.* **2**, 563–571 (2019).
61. Hastie, T., Tibshirani, R. & Friedman, J. *The Elements of Statistical Learning Data Mining, Inference, and Prediction*. (Springer, 2009). doi:10.1007/978-0-387-84858-7.
62. Yang, P. *et al.* Batch Production of 6-inch Uniform Monolayer Molybdenum Disulfide Catalyzed by Sodium in Glass. *Nat. Commun.* **9**, 979 (2018).
63. Amani, M. *et al.* Growth-substrate Induced Performance Degradation in Chemically Synthesized Monolayer MoS₂ Field Effect Transistors. *Appl. Phys. Lett.* **104**, 203506 (2014).
64. Van Der Zande, A. M. *et al.* Grains and Grain Boundaries in Highly Crystalline Monolayer Molybdenum Disulphide. *Nat. Mater.* **12**, 554–561 (2013).
65. Zafar, A. *et al.* Probing the Intrinsic Optical Quality of CVD Grown MoS₂. *Nano Res.* **10**, 1608–1617 (2017).
66. Zhang, J. *et al.* Scalable Growth of High-quality Polycrystalline MoS₂ Monolayers on SiO₂ with Tunable Grain Sizes. *ACS Nano* **8**, 6024–6030 (2014).
67. Amani, M. *et al.* Electrical Performance of Monolayer MoS₂ Field-effect Transistors Prepared by Chemical Vapor Deposition. *Appl. Phys. Lett.* **102**, 193107 (2013).
68. Pang, C. S. *et al.* Mobility Extraction in 2D Transition Metal Dichalcogenide Devices—Avoiding Contact Resistance Implicated Overestimation. *Small* **2100940** (2021) doi:10.1002/smll.202100940.
69. Khan, A. I. *et al.* Large Temperature Coefficient of Resistance in Atomically Thin Two-dimensional Semiconductors. *Appl. Phys. Lett.* **116**, 203105 (2020).
70. Lee, Y., Fiore, S. & Luisier, M. Ab Initio Mobility of Mono-layer MoS₂ and WS₂: Comparison to Experiments and Impact on the Device Characteristics. in *Technical Digest - International Electron Devices Meeting, IEDM 24.4.1-24.4.4* (IEEE, 2019). doi:10.1109/IEDM19573.2019.8993477.
71. Kozbial, A., Gong, X., Liu, H. & Li, L. Understanding the Intrinsic Water Wettability of Molybdenum Disulfide (MoS₂). *Langmuir* **31**, 8429–8435 (2015).
72. Gaur, A. P. S. *et al.* Surface Energy Engineering for Tunable Wettability Through Controlled Synthesis of MoS₂. *Nano Lett.* **14**, 4314–4321 (2014).
73. Nasr, J. R., Schulman, D. S., Sebastian, A., Horn, M. W. & Das, S. Mobility Deception in Nanoscale Transistors: An Untold Contact Story. *Adv. Mater.* **31**, 1806020 (2019).

74. Choi, H. H., Cho, K., Frisbie, C. D., Siringhaus, H. & Podzorov, V. Critical Assessment of Charge Mobility Extraction in FETs. *Nat. Mater.* **17**, 2–7 (2018).